Supporting Material:

A temperature-jump optical trap for single molecule manipulation

S. de Lorenzo,[†,‡,§] M. Ribezzi-Crivellari,[†] J. R. Arias-Gonzalez,[¶,‖] S. B. Smith,[††] and F. Ritort[†,‡,*]

[†]Departament de Física Fonamental, Universitat de Barcelona, Diagonal 645, Barcelona, Spain. [‡]Ciber-BBN de Bioingenería, Biomateriales y Nanomedicina, Instituto de Salud Carlos III, Madrid, Spain. [§]Current address, Instituto Madrileño de Estudios Avanzados en Nanociencia (IMDEA Nanociencia). Cantoblanco, 28049 Madrid, Spain. [¶]Instituto Madrileño de Estudios Avanzados en Nanociencia (IMDEA Nanociencia). Cantoblanco, 28049 Madrid, Spain. [‖]CNB-CSIC-IMDEA Nanociencia Associated Unit ‘‘Unidad de Nanobiotecnología’’, Spain. [††]Steven B Smith Engineering, Los Lunas, New Mexico, USA.

*Correspondence: ritort@ffn.ub.es

Supporting Material List

Document S1 (this document). It includes:

- Supplementary information:
    - Temperature measurement using viscosity change.
    - Estimation of the heating spot size.
    - Heating laser power measurements.
    - Heat flow model (1D, steady state)
    - Heat Flow Simulation (2D, kinetic)
    - Measuring the T-jump risetime
    - Instrument force calibration
    - Synthesis of the molecule
    - Description of the unzipping experiments
    - Simulation program for unzipping/rezipping curves
    - Experimental error on thermodynamic potentials.
- Fourteen figures.
- Three tables.

Temperature measurement using viscosity change

Stokes' law method. We measured the local temperature with a similar method to that used by Mao et al. (3) and by Peterman et al (4); namely, we used a trapped bead as a probe to detect changes in the viscosity of the water surrounding the bead. This method consists of two steps.

- We filled the fluid micro-chamber with an aqueous buffer and measured the ambient temperature of the chamber with a nearby sensor (Analog Devices AD590), which was previously calibrated against an RTD reference thermometer (Thermoworks THS-222-555). We then introduced a polystyrene bead into the calibrated optical trap. We used the motorized stage to move the chamber (and consequently the buffer fluid) in *x* and *y* axis with respect to the trapping beams and recorded the chamber velocity and force over the bead. Experimental data were plotted and linearly fitted, the slope, γ, of the regression yielding the drag coefficient at ambient temperature (Fig. S1 *a*). The viscosity at the particular ambient temperature, η_{room}, is extracted from tabulated data (1, 2), as plotted in Fig. S1 *b*.
- Using the same bead, we turned on the heating laser to a certain constant power and moved the motorized stage back and forth again while recording data of the chamber velocity and force over the bead. The slope, γ', of the linear fit is now lower because the viscosity of an aqueous solution drops with temperature (Fig. S1, *a* and *b*). The new fluid viscosity is $\eta_{room} \times (\gamma' / \gamma)$. The temperature is obtained by checking the new viscosity against tabulated data (1, 2).

This procedure removes uncertainties due to small deviations of the beads from sphericity or size errors. A Stokes' law force calibration of the instrument is carried out using pure water, however the DNA unzipping experiments are carried out in a buffer containing either NaCl (100 mM, 200 mM or 1 M) or $MgCl_2$ (10 mM or 1 mM). The ionic concentrations used in the experiments with $MgCl_2$ were so low that the viscosity of pure water was used in these cases.

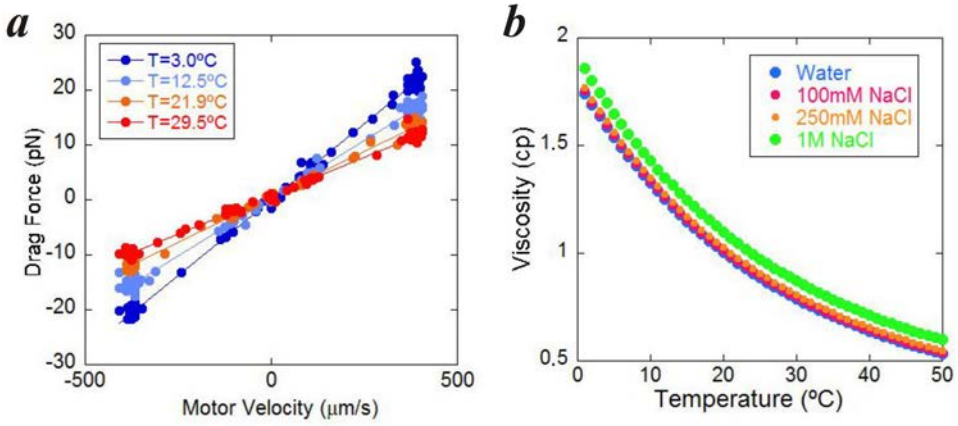

Fig. S1. Temperature measurements using viscosity changes. (*a*) Drag force vs. velocity at different powers. The corresponding temperatures, shown in the legend, were obtained as described above. The experiments were performed with a 3-μm diameter *calibration* bead in pure-water. As temperature increases the drag coefficient (proportional to the slope of the force-velocity curve) decreases. (*b*) Viscosity vs. temperature for distilled water at different [NaCl], according to two independent references, which data are similar (1, 2).

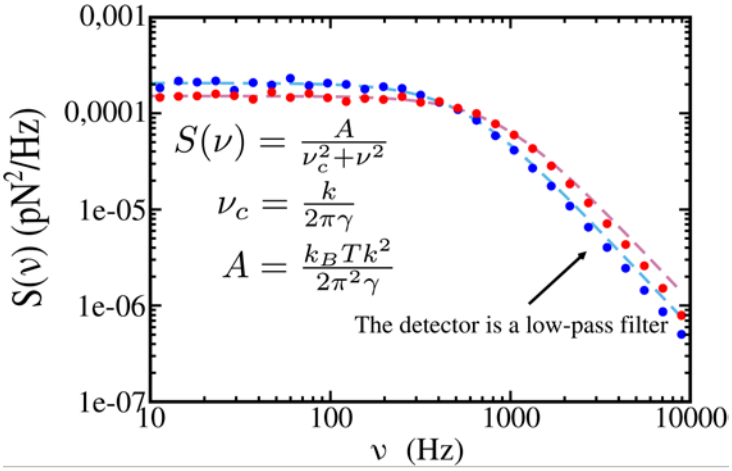

Fig. S2. Power spectrum density (PSD) of a 3-μm optically-trapped bead in distilled water. The experiments were carried out at maximum trapping (845-nm) laser power using calibration beads. Dots represent the experimental data and dashed lines are the Lorentzian fits (Eq. S1). Blue, heating laser off (fitted corner frequency, 541 Hz); red, heating laser at maximum power, 5.7 mW in the trapping region (fitted corner frequency, 859 Hz).

We also applied this method to measure the temperature rise generated by the optical trapping beams, which are weakly absorbed by water. We used both 845-nm lasers at high (80 mW) and low (20 mW) powers and observed that the difference in the drag coefficient were about 4%, which indicates a small temperature rise of 0.9-1 ºC.

Thermal noise method. The measurements of the thermal fluctuations of the trapped bead were performed at a 100-kHz acquisition rate using a Data Acquisition (DAQ) board (National Instruments PXI-1033). The analysis of the data has been carried out using the power spectrum density method (Fig. S2). This figure shows the power spectrum obtained by the Fourier transform of the thermal fluctuations, which has been fitted to a Lorentzian function,

$$\langle \Delta f^2(\nu) \rangle = S(\nu) = \frac{2\gamma k_B T \nu_c^2}{\nu^2 + \nu_c^2}, \tag{S1}$$

where ν is the frequency in Hertz, $\nu_c = \kappa/2\pi\gamma$ is the corner frequency, γ is the drag coefficient and κ is the stiffness of the trap. The stiffness of the trap when the heating laser is off is $\kappa = 0.087 \pm 0.004\, pN/nm$. If we assume that the stiffness does not depend on the temperature (see below), we can measure the viscosity from the corner frequency. The drag coefficient is obtained by imposing $\gamma = 6\pi\eta R_{eff}$, where R_{eff} is an effective radius which takes into account wall effects. Measurements with calibration beads yielded $R_{eff} = 1.77 \pm 0.04\, \mu m$. Then, temperatures can be recovered by using Vogel's formula (5):

$$T(\eta) = \frac{B}{\ln \eta - A} - C, \tag{S2}$$

where $A = -3.72$, $B = 579$ and $C = -137.5$, T is expressed in K and η in $mPa{\cdot}s$. From the temperature measurements in Fig. 3 *b* (main text), we can now check the hypothesis that the trap stiffness does not depend on the temperature. Using the relation $\kappa = \pi A/\nu_c k_B T$, where $A = k_B T k^2/2\pi^2\gamma$ and ν_c are extracted from the fitted data, we observe in Fig. S3 no systematic effect of the temperature or the position in the stiffness values.

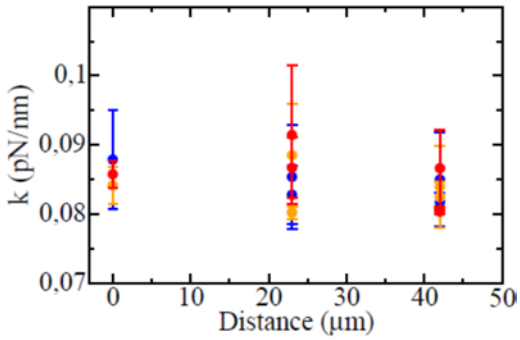

Fig. S3. Effect of temperature on trap stiffness. The graph shows measurements at different positions (see inset of Fig. 3 in the main text for details) and at different heating laser powers inside the fluidics chamber: red dots, 5.7 mW, yellow dots, 4 mW and blue dots, 0 mW (heating laser off).

Vogel's formula can be avoided if we measure the temperature from the force-fluctuations measurements. Specifically, we can use $T = \pi A/\nu_c k_B \kappa$ and the fitted parameters $A = k_B T k^2/2\pi^2\gamma$ and ν_c to obtain temperature data, assuming again that the stiffness does not depend on the force. With this thermometry method we do not require viscosity data but we have to measure the low-signal force fluctuations, which are prone to both calibration errors and distortions by low frequency noises.

The results of this analysis are shown in the graph below (Fig. S4). With the statistics obtained in these measurements, we cannot obtain a reliable temperature measurement. Nevertheless the measured temperature agrees qualitatively well with what was obtained using Vogel's formula and the thermal noise analysis. It is expected that with larger statistics the agreement improves.

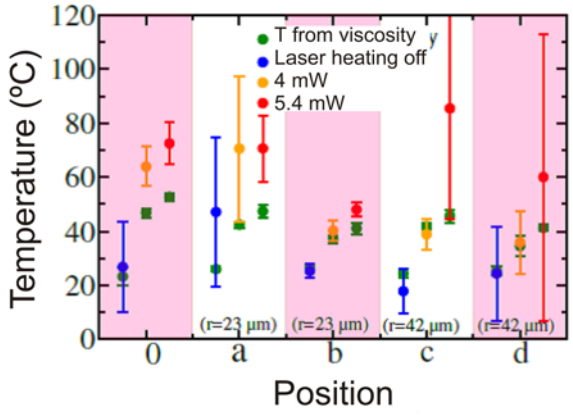

Fig. S4. Results of Temperature vs Distance from the center of the heating laser spot and comparison with the Vogel results. Heating laser powers are inside the fluidics chamber.

Estimation of the heating spot size

To determine the size of the Köhler illumination cylinder, we examine next the heating laser beam path before the microfluidic chamber (Fig. S5). As depicted, the heating laser light is coupled to the optical axis in our setup through an SM-28 optical fiber. Light exits the fiber in a cone with vertex angle θ such that the beam numerical aperture is $NA = sin(\theta/2) = 0.14$. The light cone expands over ~8.2 mm until it reaches an

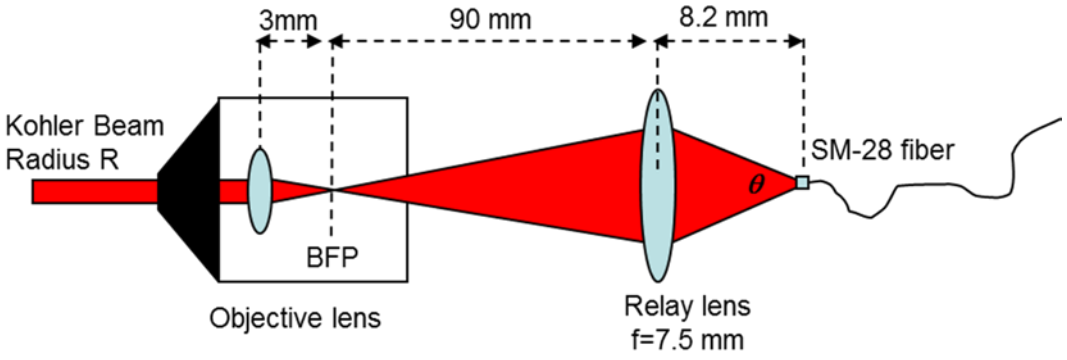

Fig. S5. Heating laser optical path. The beam expands from a single-mode optical fiber (SM-28) with a numerical aperture (NA) of 0.14 until a relay lens, where it is focused along 90 mm onto the back focal plane (BFP) of the first objective lens. Then, the narrow beam (NA=0.011) expands until it hits the 60X objective lens with effective focal length = 3 mm, where it is collimated into a cylinder with radius R=33μm, travelling across the microfluidics chamber until it reaches the front of the opposite objective lens (see the text for details). Three wavelengths (a blue LED illuminating the chamber, two counter-propagating 845-nm trapping lasers and a 1435-nm heating beam) share the optical path across the microfluidics chamber. Both the heating beam and the trapping laser that travels in the same direction are collected by the second objective lens and imaged onto a CCD camera. The wavelength of the heating laser is not visible with a silicon-target CCD; therefore a 905-nm auxiliary laser is incidentally used to estimate the size of the hot spot on the TV screen and to align it relative to the optical trap spot.

adjustable relay lens (Thorlabs CFC-8X). Then, the light is focused, entering the objective as a slightly convergent cone with initial radius of ~0.14×8.2 ≈ 1 mm. The relay lens distance can be tuned at ~90 mm for conjugate focusing to the back-focal plane (BFP) of the first objective. The numerical aperture of the convergent cone is thus $NA \approx 1/90 = 0.011$. Since the focal length of the objective lens is ~3 mm, the radius of the Köhler illumination cylinder is R ≈ 0.011 × 3 mm ≈ 33 μm.

Heating laser power measurements

We used a Thorlabs PM100 power meter with a Germanium slim photodiode power sensor (Thorlabs S132A) to determine how much heating power was delivered to the Köhler heating beam. Cargille immersion fluid (6) was used inside the chamber as well as between the microchamber and the objective lenses. An alignment check of the heating spot was conducted using a 905-nm laser, which can be monitored on a TV screen. The Germanium probe was installed between the prism box and the first objective lens. The process was repeated at the left objective lens exit.

At maximum laser current, the measured power after the second objective was 3.48 mW with Cargille fluid in the chamber. Therefore the input must have been 3.46 / 0.03125 = 111 mW. Although the maximum rated output for our heating laser is 160 mW, that power must then pass through 2 meters of optical fiber, a collimator lens, a dichroic mirror and two polarizing beamsplitter cubes before entering the first objective. Since each objective lens is identical, the maximum power in the center (Köhler heating beam) must have been $\sqrt{111 \times 3.48} = 19.7\,mW$. Note each objective lens transmits only 17.7% at 1435 nm.

TABLE S1 Heating-laser power measured at various points.

Switch positions	1	2	4	6	7	8	10	14	15
Drive current	91	167	295	400	445	482	555	670	695
Power in	11.7	25	47	65	72	(78.7)	(90.2)	(108)	(111)
Power out	0.36	0.76	1.48	2.02	2.25	2.46	2.82	3.38	3.48

First row indicates switch positions on laser power supply, which in the steady state yield a constant drive current (second row, in milliamperes) into heating laser. Third row shows power (milliwatts) entering first objective lens. Final row shows power (milliwatts) exiting 2nd objective lens after passing through chamber which was filled with Cargille fluid (absorbs nothing at 1435 nm). Due to sensor saturation it was not possible to measure more than 72 mW with the Thorlabs S132A probe. Therefore the larger input powers (shown in parentheses) were estimated from the corresponding output powers assuming a constant attenuation ratio (output/input) = 0.03125.

Now suppose we load water into the microchamber instead of Cargille fluid. Then the power in the beam will be partially absorbed and the transmitted power will follow Beer's law: $I(x) = I(0)\cdot\exp(-ax)$. Note that α, the absorption coefficient for water, is about 31.4 cm^{-1} (7) and the thickness of water in a typical chamber is 0.011 cm. Therefore the transmission will be 71% and the absorption 29%. Assuming maximum laser power where $I(0)$ = 19.7 mW , the absorbed power will be 5.7 mW.

Heat flow model (1D, steady state)

We assume that the heat flows radially, perpendicular to the laser beam axis and outward the Köhler-illumination geometry, as defined by a cylinder of radius R and length L. The *heat power* transferred across two coaxial cylindrical surfaces with radii r and $r + dr$ is:

$$P = -\kappa A \frac{dT}{dr}, \tag{S3}$$

where P is the light power absorbed by water, κ is the thermal conductivity of water, A is the surface area of the cylinder ($A = 2\pi rL$) and dT is the temperature change between the two cylindrical surfaces. The *heat flux density* (power per unit area) through the shell surface is equal to the total light power absorbed inside the shell divided by the surface area of the shell, $Q = P/A$. Eq. S3 then reads

$$dT = -\frac{Q}{\kappa} dr. \tag{S4}$$

The heat flux density is:

$$Q = \begin{cases} \dfrac{Pr}{2\pi R^2 L}, & r \le R, \quad \text{(S5A)} \\ \dfrac{P}{2\pi r L}, & r > R\,. \quad \text{(S5B)} \end{cases}$$

Integrating Eq. S5A for $0 < r < R$ and Eq. S5B for $< r < +\infty$, we obtain

$$T(r) = \begin{cases} T_0 - \dfrac{P}{4\pi L\kappa}\dfrac{r^2}{R^2}, & r \le R, \quad \text{(S6A)} \\ T(R) - \dfrac{P}{2\pi L\kappa}\ln\dfrac{r}{R}, & r > R\,, \quad \text{(S6B)} \end{cases}$$

where 'ln' is the natural logarithm. To apply the boundary conditions, on the one hand, we note that integrating dT outside the radius R to a distance r=+∞ yields an infinity temperature drop. The usual procedure in such problems is to cut off the integration at r=L, the length of the cylinder. Then, $T(L) = T_{room}$ in Eq. S4B implies that $T(R) = T_{room} + (P/2\pi L\kappa)\ln(L/R)$, being T_{room} the room temperature. On the other hand, we must impose the continuity at $r = R$, which implies that $T(R) = T_0 - (P/4\pi L\kappa)$. Therefore, the constant T_0 in Eq. S4 is given by:

$$T_0 - T_{room} = \frac{P}{2\pi L\kappa}\left(\ln\frac{L}{R} + \frac{1}{2}\right). \tag{S7}$$

By defining the temperature increment with respect to the ambient temperature, $\Delta T = T - T_{room}$, we express the solution of the problem as follows:

$$\Delta T(r) = \begin{cases} \dfrac{P}{2\pi L\kappa}\left[\ln\dfrac{L}{R} + \dfrac{1}{2}\left(1 - \dfrac{r^2}{R^2}\right)\right] & r \le R, \quad \text{(S8A)} \\ \dfrac{P}{2\pi L\kappa}\ln\dfrac{L}{r}, & r > R, \quad \text{(S8B)} \end{cases}$$

In our experimental configuration, P=5.7 mW at the maximum laser power (see section above), the distance between the chamber walls is L≈100 μm, the radius of the heating cylinder, R=33μm (previous section), the thermal conductivity of water $\kappa \approx$ 0.58 W/m·K and the ambient temperature, T_{room}=25 ºC. The blue line in Fig. S6 plots Eq. S8 under these conditions.

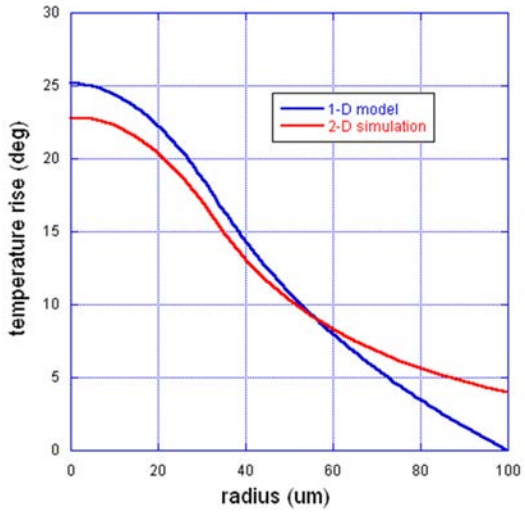

Fig. S6. Temperature profiles derived from different models. Blue line: 1D model where input power is 5.7 mW, L=100 μm and R=33 μm. Red line: 2D simulation where input beam power is 19.7 mW so 29% = 5.7 mW is extracted according to Beers law. R=30 μm and L=110 μm.

Heat Flow Simulation (2D, kinetic)

A heat-flow simulation was created that uses finite elements with specified material properties, e.g. for water, glass and Cargille fluid. In contrast to the 1D model above, each element in this 2D model is specified by a radius plus a lateral position parallel to the optic axis. Such ring-shaped elements can extend through the water, chamber walls, immersion fluid and up to the objective lenses. No arbitrary cutoff is required in the radial direction to limit the temperature rise at the center because lateral heat flow serves as a radial cutoff.

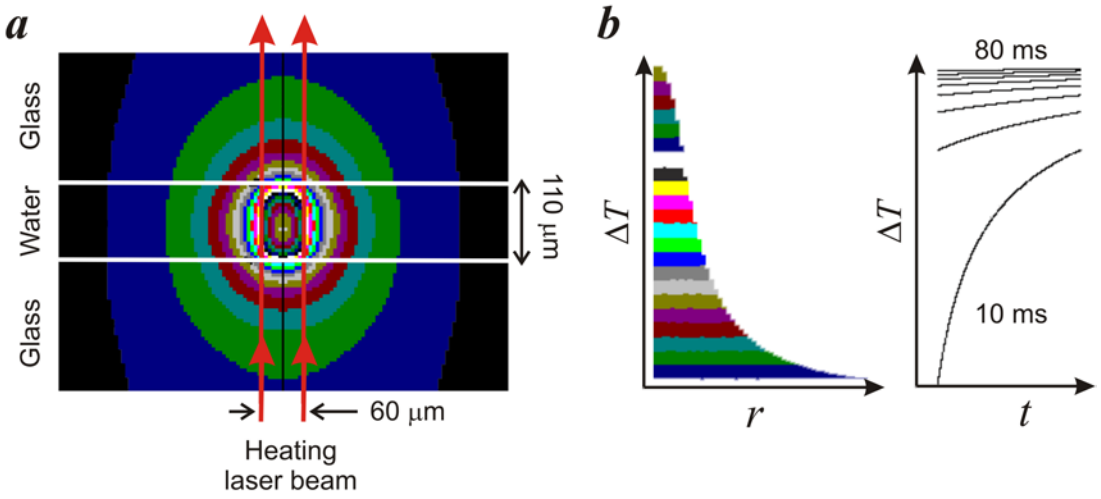

Fig. S7. Simulated heating pattern. (*a*) Temperature distribution due to radiation absorbed at the intersection of a 60 μm diameter heating laser beam and 110 μm water layer. Glass coverslips are drawn at top and bottom regions. Black color indicates a temperature rise less than 1 °C above ambient. Each new color represents an additional 1-degree rise. (*b*) Left, radial temperature profile in multiple colors. Such profile grows in height with time. Right, black curves follow the temperature at the center of the beam versus time. Each curve segment spans a time of 10 ms. Here, 8 successive curves represent 80 ms during which the center temperature has reached a steady state. In this example at time=30 ms the simulated temperature reached 90% of its final value, and at time=80 ms it reached 98%.

Our 2D simulation, Figs. S6 and S7, is "kinetic" because the finite elements have specific heat capacities and it takes time for heat to flow into an element by conduction and the temperature to rise. Heat is conducted both radially and laterally between adjacent rings. Time progresses in 4-μm steps, thus allowing characterization of transient responses when the heating beam is instantly turned on.

Source code and sample outputs can be downloaded at http://tweezerslab.unipr.it/cgi-bin/mt/software.pl/Search.

Measuring the Temperature-jump risetime

The temperature-jump rise time can be checked by using a DNA hairpin as a local thermometer. To do this we held the trap position constant while measuring the equilibrium rezip/unzip force while the temperature changed. Figure S8 shows the unzipping force of a DNA hairpin during a time when the heating power was altered by changing the heating-laser drive current. Under these conditions the risetime was about 200 ms which is 7 times longer than predicted by the simulation. Note the laser power supply had an RC filter to prevent sudden changes in the drive current. That filter comprises a 1 ohm metering resistor, 1 ohm dynamic laser-diode resistance, and a 0.056 farad capacitor. Then RC = 2×0.056 = 0.112 seconds. Therefore we were not able to observe the intrinsic delay for heating the water and glass chamber with an instant power pulse.

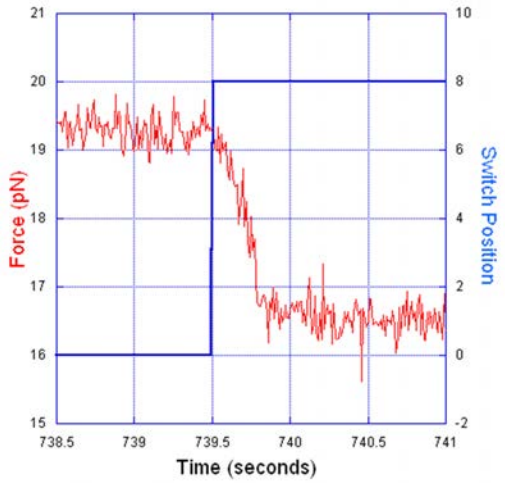

Fig. S8. Measurement of temperature rise-time. Red line is equilibrium zip/unzip force of DNA hairpin in 100 mM NaCl, at 5 ^{o}C above ambient. Blue line indicates switch position on heating laser power supply. Switch=zero delivers zero drive current into heating laser. Switch=8 initiates a drive current of 482 mA (see table S1).

Instrument force calibration

The calibration of force through viscosity changes was performed in a chamber with pure water using polystyrene microspheres that are specific for calibration, with a precise diameter (Polyscience ref Microbead Nist Traceable particle size standard 3.00 µm Cat# 64060 - DISC calibration). These microspheres have a nominal diameter of 3.00 ± 0.07µm. A single peak in the centrifuge insures a single peak in the size distribution. Our bead distribution has CV = 2.2%. Measuring a set of N beads will reduce the likely error (computed mean minus true mean) by a factor of $\sqrt{N}$. Reducing our likely error down to a 1% requires measuring five beads on average.

To make one such measurement, a single microsphere is captured in the optical trap. The micro-chamber is mounted on a stage platform in the optical tweezers instrument that can be moved along the *x*-*y*-*z* axis. By measuring the velocity at which the chamber is moved and by knowing the viscosity of water and the size of the bead, it is possible to calculate the force on the particle using Stokes' law (Fig. S9 *a*). This method is used to calibrate force along each axis (x, y, z). Usually the drag coefficients for a bead are in good agreement for all three directions. However if the trapped bead is oblate, or it has some dirt attached, then the *z*-axis drag appears lower because the extra bead mass aligns with the trapping-beam axis (*z*-axis) and this configuration presents lower fluid drag in the *z*-axis direction. Such beads can be excluded from the calibration.

Stokes' law measurements have been carried out using both the old and new microchamber designs (Fig 2*a*, main text). Interestingly, our experimental results, Fig. S9 *b*, demonstrate that if we use the Stokes' law as a method of force calibration, the proximity of the bead to the wall of the microchamber coverglass is an important aspect to consider. This effect, known as Faxen's law, could be defined as a correction to the shear viscosity and viscous drag coefficient of a microsphere in a viscous fluid sitting close to a wall (8). In our case, the bead in the trap is in close proximity to the two coverglass walls comprising the microchamber. For this reason we have corrected the expression for the viscous drag coefficient by using the Happel correction (9) for a microsphere of radius *r* and separation between walls of 2*h*:

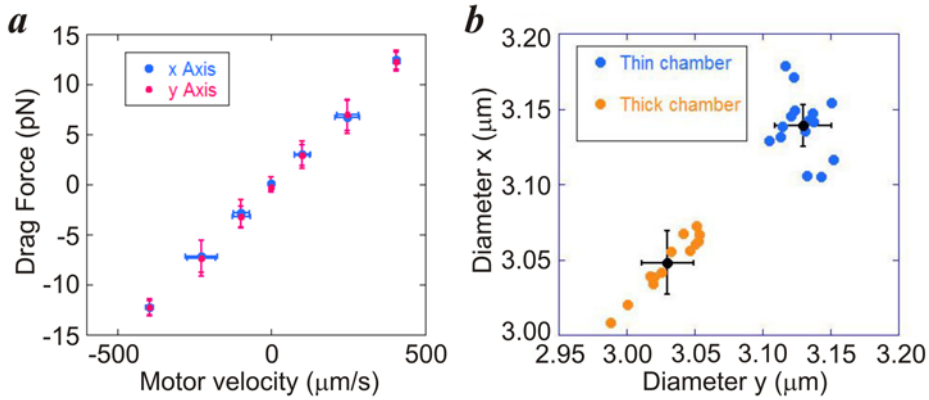

Fig. S9. Force calibration using Stokes' law. (*a*) Drag force vs motor velocity in x and y axes. Experiments were performed in pure water using special microspheres for calibration. The points showed in this graph correspond to a single bead and have been obtained by taking the average over the raw data. (*b*) Diameter measured along the x-axis vs diameter along y-axis by Stokes' law using the standard expression for the drag coefficient $\gamma = 6\pi\eta r$ where *r* is the bead radius. Data were obtained by measuring over 10/15 beads. The mean diameter measured in the thick chamber along the x-axis is 3.05 ± 0.019 μm and 3.03 ± 0.021 μm along the y-axis. The mean diameter measured in the thin chamber along the x-axis is 3.14 ± 0.021 μm and 3.13 ± 0.014 μm along the y-axis. Two different batches of calibration beads were tested with the same results. The difference observed between mean diameters evidences the importance of the Happel correction to the drag coefficient.

$$\gamma = \frac{6\pi\eta r}{1 - 1.004(r/h) + 0.418(r/h)^3 - 0.21(r/h)^4 - 0.169(r/h)^5} \qquad \text{(S9)}$$

Equation S9 predicts a change of a +3% for a 3-μm diameter bead in a 100-μm thick chamber. Therefore this correction was necessary for accurate calibration.

As formerly described (10, 11), the calibration of a momentum-flux force sensor depends on the sensitivity of its position-sensitive photodetector. In our instrument, both the fluid chamber and the silicon detectors cool to 4 ºC when the instrument head is lowered into the icebox. Therefore we did an experiment to check the force calibration at low temperatures by measuring the Stokes drag force on our calibration beads in cold conditions (4 ºC water, heating laser off). We found that the photodetector reading increased by a factor of 1.69 over the case where the photodetector and water were held at room temperature (25 ^{o}C). However literature values (2) show that water viscosity increases by a factor of 1.76 between those two temperatures. Therefore the momentum sensor under-reported the test force by ~4% of reading at low temperature, consistent with such a reduction in photodetector sensitivity. Thus the force calibration must be corrected by +4% for *cold experiments* compared to *hot experiments*, regardless of the state of the heating laser, which does not affect the detectors.

Synthesis of the molecule

The molecular construct consists of a long, 6838-bp DNA stem from λ-DNA (12) (New England Biolabs) with a tetraloop at the end of the hairpin (Fig. S10). To extract the DNA segment, a digestion of the λ-DNA phage with the BamHI restriction enzyme was carried out. The target of BamHI (New England Biolabs) is 5'-GGATCCC-3' and therefore this enzyme cleaves λ-DNA at several specific places. We are interested in the

segment between 41,732−48,502 bases, which forms the stem of the DNA hairpin (the cosR end). The DNA stem, the two 29-bp handles (13) and the tetraloop (3'-ATCA-5') are ligated to the cosR end and the previously modified Bam HI end. The role of the tetraloop is to prevent the separation of the two strands when the DNA hairpin is unzipped. To join the tetraloop, a self-complementary oligonucleotide, which forms a tetraloop on one side and a cohesive Bam HI end at the other, is ligated to the BamHI end of the DNA construction. To generate the DNA handles, an oligonucleotide (previously modified with several digoxigenins by using DIG Oligonucleotide Tailing Kit, 2nd Generation, Roche) is hybridized with a second 5' biotin-modified oligonucleotide. This DNA construction is complementary to cosR end and two identical 29-nucleotide long ssDNA at the other end. The two ssDNA are hybridized with a third oligonucleotide which is complementary to them resulting in two dsDNA handles. These handles are attached to the DNA construction by ligation reaction. The sample is kept in a 10-mM Tris-HCl, 5-mM EDTA buffer.

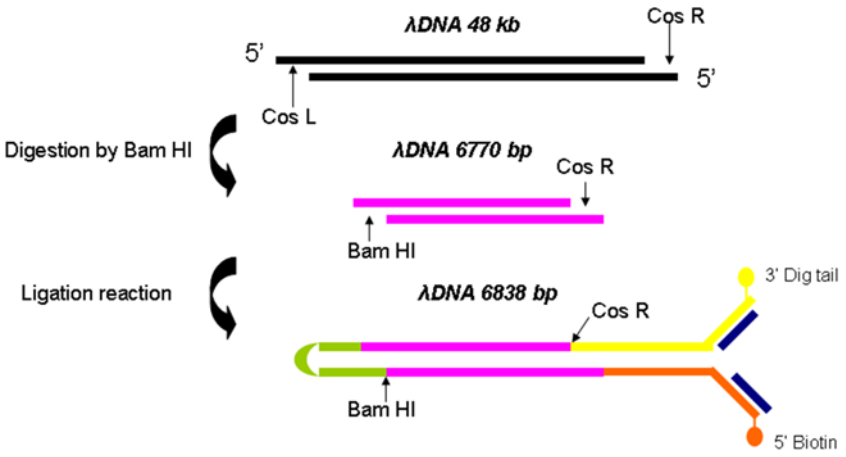

Fig. S10: Scheme of the synthesis of the DNA hairpin with closing tetraloop and dsDNA handles for the optical tweezers experiments.

The two handles are functionalized with biotin on one side and digoxigenin on the other. To unzip DNA, the DNA construction is attached to two polystyrene beads. One bead is coated with Streptavidin (SA) (G.Kisher GbR, ∅=2.0-2.9μm). The SA bead binds to the biotin-labeled handle of the molecular construction. The other microsphere is coated with protein G (Spherotech, Libertyville; ∅=3.0-3.2 μm), which is in turn cross-linked covalently with the anti-digoxigenin (AD) (Roche Applied Science) polyclonal antibodies through DMP. The AD bead binds to the digoxigenin labeled handles. To ease the binding between the hairpins and the AD beads, they are incubated together for 15 min in a TE buffer solution.

Description of the unzipping experiments

The unzipping experiments were carried out using the above explained DNA molecular construction in TE buffer (Tris 10 mM, pH 7.5) supplemented with either NaCl (1 M and 100 mM) and 1-mM EDTA or $MgCl_2$ (10 mM and 1 mM) as follows:

An SA bead is fixed on the tip of the micropipette by air suction and an AD bead is optically trapped (Fig. S11). The optical trap is moved relative to the bead fixed in the micropipette and the distance between them decreases until the beads rub together.

Then, by moving the beads apart, it is possible to check if the connection between the hairpin and the two beads has been created. DNA unzipping is generated by increasing the force applied to the strands of the molecule. When the applied forces reach a critical value, basepairs are disrupted hence creating the characteristic sawtooth pattern (see Fig. 4 *a* in the main text). This pattern is composed of peaks of different shapes and sizes (12). Pulling rates were about 50 nm/s . When the molecule was fully unzipped, the elastic response of the ssDNA was observed at the end of the curve.

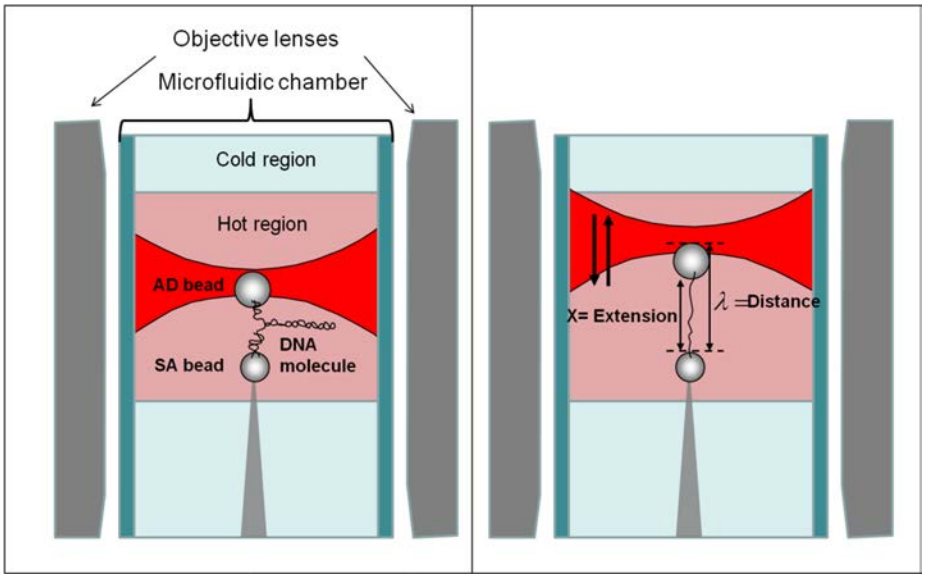

Fig. S11. Schematic representation of the unzipping experiments (not to scale). The light red ("hot region") corresponds to the volume heated by the heating laser. The light blue ("cold region") is the volume at ambient temperature.

Simulation program for unzipping/rezipping curves

Program Tweez13E is a Brownian dynamics simulation for the mechanical zipping of a DNA hairpin molecule attached to a bead in an optical-trap. The output is a Force-Distance Curve (FDC) characteristic of the chosen base sequence and input temperature. Different pull/relax cycles exhibit slightly different FDCs due to randomly generated thermal forces (Fig. S12). Pull / relax cycles also display force hysteresis that increases with pulling speed. Below is a simplified code example from the main loop:

```
repeat
   time:=time+dt ;      {dt = 1e-6 sec}
   getMoleculeTension;  {bead position, chain length, WLC model}
   zipHairpin(tension); {move fork position up or down 1 basepair}
   sumForcesOnBead;     {molecule tension + Brownian + optical}
   moveBeadInTrap;      {Langevin Eqn for overdamped particle}
   trackLightForce;     {assumes linear trap, stiffness = kSpring}
   moveTraps;           {to scan through length of molecule}
until scan=finished
```

The simulation programs can be downloaded from http://tweezerslab.unipr.it/cgi-bin/mt/software.pl/Search. They were written and compiled with Borland Turbo Pascal 7 and they will run on most 32-bit PC computers with an XP operating system.

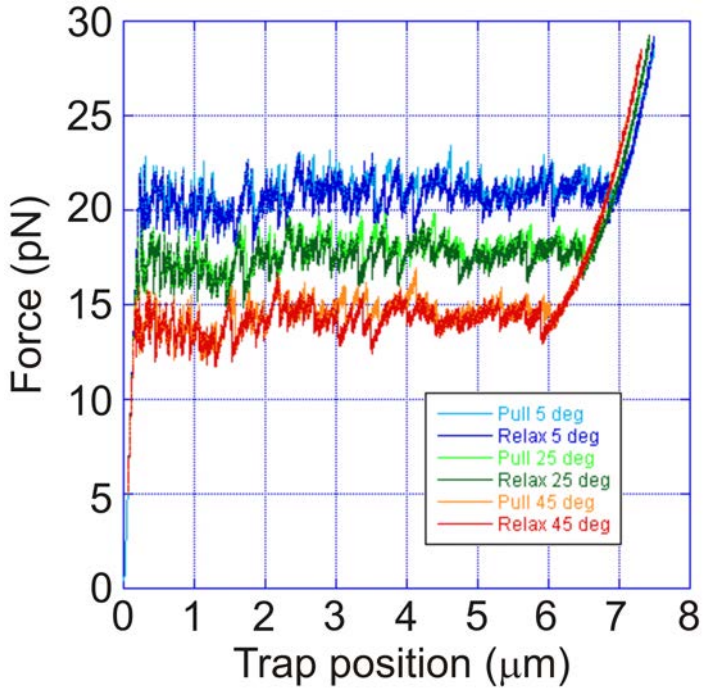

Fig. S12. Simulation output from TWEEZ13E for a 6.8-kbp hairpin assuming Santa Lucia et al. 1998 energy values in 1 M NaCl. Note that the ssDNA curves at the right end are longest for low temperature (blue) and shortest for high temperature (red). This is an example of rubber elasticity using the extensible-FJC model with a constant Kuhn-segment length. Therefore the experimental behavior (Figs. 4 *a* and 7 *a* in the main text) is surprising because there all the ssDNA extensions coincide above 25 pN, regardless of temperature.

Experimental error on thermodynamic potentials.

The homogeneous base-pair free energy was determined from the integral of the ssDNA FDC in the main text:

$$\Delta G_0 = \int (\Delta x/\mathrm{bp})\, df = L_c \int \left[\coth\left(\frac{f L_K}{k_B T}\right) - \frac{k_B T}{f L_K}\right]\left(1 + \frac{f}{K}\right) df \qquad \text{(S10)}$$

The four measured parameters are the mean unzipping force, f, the Kuhn length, L_K, the contour length, L_0, and the stretch modulus, K. Their errors affect the uncertainty in our free energy measurements. In Fig. S13 *a*, we show the different contributions to the free energy error as a function of f assuming a 5% relative error in the different parameters. These contributions to the error are computed by propagation:

$$d\Delta G_0 = \frac{\partial \Delta G_0}{\partial \alpha_i} d\alpha_i, \qquad \text{(S11)}$$

with $\alpha_i = f, L_K, L_0, K$. The uncertainty in force measurement is clearly the dominant term, the other ones having a low influence in the total error. A similar approach can be used to estimate the relevance of the force-dependent elastic contribution to the entropy change:

$$\Delta S_{elas} = \int \frac{\delta(\Delta x/\mathrm{bp})}{\delta T} df\,. \qquad \text{(S12)}$$

This entropy contribution can be rewritten as:

$$\Delta S_{elas} = -\frac{\partial \Delta G_0}{\partial L_K}\frac{\partial (L_K/k_B T)}{\partial T} - \frac{\partial \Delta G_0}{\partial K}\frac{\partial K}{\partial T}. \quad \text{(S13)}$$

From Fig. S13 *b* we conclude that $L_k/k_B T$ and K do not vary more than 10% over the temperature range we explored so we can estimate $\partial K/\partial T < 2\ pN/K$ and $\frac{\partial (L_K/k_B T)}{\partial T} = 0.0003\ (pN\ K)^{-1}$. With these estimations, we provide upper bounds to the elastic contributions to the entropy and validate the fact that we neglected these contributions in the main text.

In Fig. S13 *b* we show the two different contributions to ΔS_{elas} (one for $L_k/k_B T$ and one for K). Clearly the elastic contribution to the entropy change is below the experimental error on the total entropy change measured via the Clausius-Clapeyron equation and can be neglected in our measurements of ΔS_0.

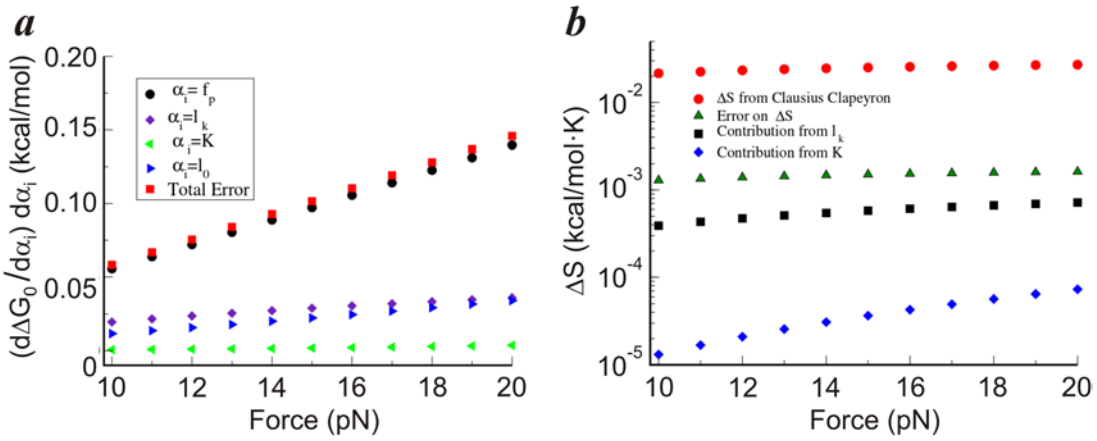

Fig. S13. Error contributions to thermodynamic potentials as a function of force. (*a*) Free energy change. (*b*) Entropy change.

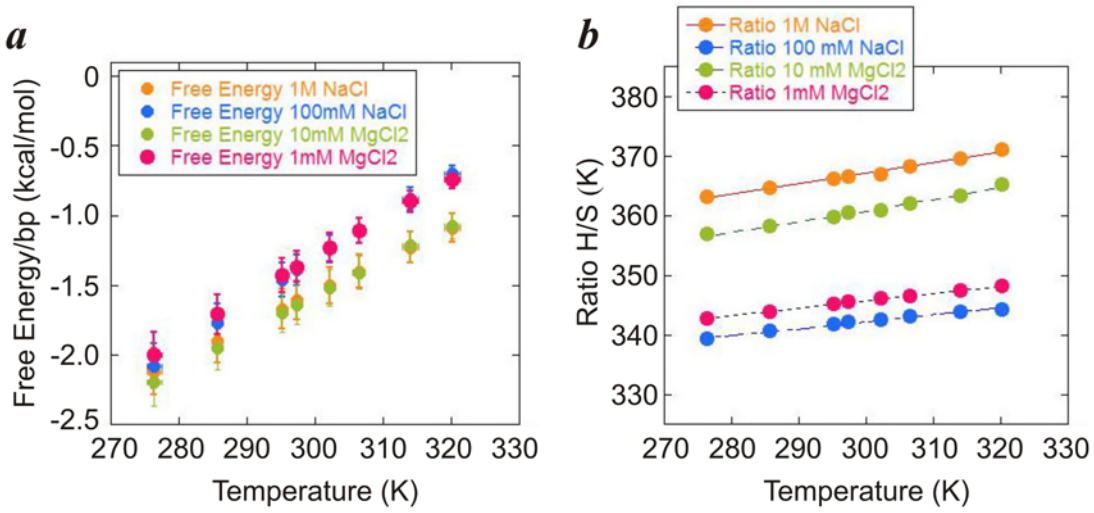

Fig. S14. (*a*) Base-pair free energies at different salt conditions. (*b*) Ratio between enthalpies and entropies at different salt conditions.

TABLE S2 Relation between the mean Mean Force and the temperature.

	Mean Force		
T (ºC)	**Exp results**	**HU Prediction**	**UO Prediction**
5	20.6 ± 0.5	19.9 pN	20.9 pN
15	18.9 ± 0.1	18.4 pN	19.2 pN
25	17.2 ± 0.3	16.9 pN	17.6 pN
35	15.4 ± 0.4	15.4 pN	16.0 pN
45	13.7 ± 0.5	13.9 pN	14.3 pN

Experimental data combined with two theoretical predictions. Exp results (Experimental results), HU Prediction (Based on unzipping measurements, Huguet et al. 2010), UO Prediction (Unified Oligonucleotide based on bulk melting measurements, Santa Lucia et al. 1998). The mean values of the experimental results were obtained averaging over 8 molecules at 1 M NaCl condition of salt.

TABLE S3 Thermodynamic potentials at room temperature (298K).

	F (pN)	Δx/bp (nm)	ΔG/bp (kcal/mol)	ΔS/bp (kcal/(mol K))	ΔH/bp kcal/mol
			1 M NaCl		
Exp values	17.1 (0.8)	0.95 (0.06)	-1.61 (0.15)	-23 (1.)	-8.5 (0.4)
HU values	16.9 (0.8)	0.95 (0.06)	-1.6 (0.14)	-20 (1.)	-7 (0.4)
UO values	17.6 (0.9)	0.95 (0.06)	-1.7	-22.1	-8.3
			100 mM NaCl		
Exp values	14.6 (0.7)	0.94 (0.04)	-1.38 (0.11)	-31. (1.3)	-10.6 (0.4)
HU values	14.8 (0.7)	0.94 (0.04)	-1.3 (0.14)	-20. (1.)	-8 (1)
UO values		0.94 (0.04)	-1.4	-23	-8.3
			10 mM $MgCl_2$		
Exp values	17.1 (0.8)	0.95 (0.06)	-1.6(0.14)	-26.(1.4)	-9.3 (0.4)
HU values	16.7 (0.8)	0.95 (0.06)	-	-	-
UO values		0.95 (0.06)	-1.7	-22.0	-8.3
			1 mM $MgCl_2$		
Exp values	14.6 (0.7)	0.94 (0.04)	-1.36 (0.11)	-28.4 (1.4)	-9.8 (0.4)
HU values	15.1 (0.7)	0.94 (0.04)	-	-	-
UO values		0.94 (0.04)	-1.4	-22.1	-8

Comparison between experimental (Exp Values) and theoretical (UO and HU, where available) values for the thermodynamic potentials at room temperature in four salt conditions (1 M NaCl, 100 mM NaCl, 10 mM $MgCl_2$ and 1 mM $MgCl_2$). HU refers to the prediction by Huguet et al. (2010), UO refers to the prediction by the MFOLD server, based on (14, 15). The temperature dependence of the measured thermodynamic potentials is shown in Fig. 8.

Supporting References

1. Ozbek, H. 2010. Viscosity of aqueous sodium chloride solutions from 0ºC-150ºC. Lawrence Berkeley National Laboratory. Paper LBL-5931.
2. Swindells, J. F. 1982. Handbook of Chemistry and Physics CRC 62edition. National Bureau of Standards.
3. Mao, H., J. R. Arias-Gonzalez, S. B. Smith, I. Tinoco, Jr., and C. Bustamante. 2005. Temperature control methods in a laser tweezers system. Biophys J 89:1308-1316.
4. Peterman, E. J., F. Gittes, and C. F. Schmidt. 2003. Laser-induced heating in optical traps. Biophys J 84:1308-1316.
5. Vogel, H. 1921. The law of the relation between the viscosity of liquids and the temperature. Phys. Z. 22:645-646.
6. Series AAA n=1.33 ref "AST3421, June 2, 2003. Typical Characteristics". Cargille Laboratories Inc., 55 Commerce Rd. Cedar Grove, NJ. 07009 USA.
7. Palmer, K. F., and D. Williams. 1974. Optical properties of water in the near infrared. J. Opt. Soc. Am. 64:1107-1110.
8. Svoboda, K., and S. M. Block. 1994. Biological applications of optical forces. Annu Rev Biophys Biomol Struct 23:247-285.
9. Happel, J., and H. Brenner. 1983. Low Reynolds Number Hydrodynamics: With Special Applications to Particulate Media. Springer Netherlands.
10. Bustamante, C., and S. Smith. 2005. Light-force sensor and method for measuring axial optical-trap forces from changes in light momentum along an optic axis. U.S.A. patent 7, 133, 132, B2.
11. Smith, S. B., Y. Cui, and C. Bustamante. 2003. Optical-trap force transducer that operates by direct measurement of light momentum. Methods Enzymol 361:134-162.
12. Huguet, J. M., C. V. Bizarro, N. Forns, S. B. Smith, C. Bustamante, and F. Ritort. 2010. Single-molecule derivation of salt dependent base-pair free energies in DNA. Proc Natl Acad Sci U S A 107:15431-15436.
13. Forns, N., S. de Lorenzo, M. Manosas, K. Hayashi, J. M. Huguet, and F. Ritort. 2011. Improving signal/noise resolution in single-molecule experiments using molecular constructs with short handles. Biophys J 100:1765-1774.
14. SantaLucia, J., Jr. 1998. A unified view of polymer, dumbbell, and oligonucleotide DNA nearest-neighbor thermodynamics. Proc Natl Acad Sci U S A 95:1460-1465.
15. Peyret, N. 2000. Prediction of Nucleic Acid Hybridization: Parameters and Algorithms PhD dissertation. In Department of Chemistry. Wayne State University, Detroit, MI.